Atmospheric correction for global mapping spectroscopy: ATREM advances for the HyspIRI preparatory campaign

David R. Thompson [a,*], Bo-Cai Gao [b], Robert O. Green [a], Dar A. Roberts [c], Philip E. Dennison [d], Sarah R. Lundeen [a]

[a] Jet Propulsion Laboratory, California Institute of Technology, Pasadena, CA, United States
[b] Naval Research Laboratory, Washington, DC, United States
[c] University of California, Santa Barbara, CA, United States
[d] University of Utah, Salt Lake City, UT, United States

ABSTRACT

Orbital imaging spectrometers, such as the proposed Hyperspectral Infrared Imager (HyspIRI) mission, will provide global, multi-year Visible Shortwave Infrared (VSWIR) reflectance maps. Monitoring the Earth's surface at high spectral resolution will advance our understanding of changing ecosystems and land use. These applications depend on reliable correction of atmospheric scattering and absorption. The HyspIRI Preparatory Campaign is an airborne precursor mission comprised of multiple flights by the "classic" Airborne Visible Infrared Imaging Spectrometer (AVIRIS-C) over a wide geographic area. This article describes the atmospheric correction that we have implemented for the campaign. We first present the theoretical basis of our approach, which is grounded in the ATmospheric REMoval (ATREM) algorithm. We then describe new enhancements including retrieval of pressure altitude, which improves accuracy over widely varying topography, and joint retrieval of optical absorption for three phases of water (vapor, liquid, and ice), which improves accuracy over vegetated areas. Reflectance is validated using ground spectra acquired across a wide range of targets and elevations. Finally, we use the algorithm to map vapor, liquid, and ice phases of water over 6 months across a 14,000 km^2 region of California.

© 2015 Elsevier Inc. All rights reserved.

1. Introduction

Orbital imaging spectrometers such as the proposed Hyperspectral Infrared Imager (HyspIRI) mission (Green, Painter, Roberts, & Dozier, 2006) will significantly advance our understanding of long-term changes in ecosystems and land use. Global measurements from a Visible Shortwave Infrared (VSWIR) imaging spectrometer, producing contiguous spectra spanning 380–2510 nm often called "hyperspectral," will enable diverse data products such as maps of plant species, physiology and chemistry over land, and phytoplankton ecosystems over oceans. These data will provide unique insight into the Earth's ecological responses to climate change. An orbital mapping instrument will face new challenges beyond those of more spatially limited airborne missions. First, the data will cover a wide range of terrain and atmospheric conditions. Consistent estimates of surface properties require accurate atmospheric correction across time, variable elevation, and atmospheric attenuation gradients. Second, global mapping instruments produce large data volumes: over 5 Tb/day for the HyspIRI reference design (Hook & Oaida, 2010). This makes human intervention impractical, so atmospheric corrections must operate automatically.

Third, the common practice of improving atmospheric correction with in-scene reference targets is not feasible for global missions. For these reasons, further maturation of atmospheric correction methods will be important to exploit global datasets.

The 2013–2014 HyspIRI Preparatory Campaign aims to demonstrate relevant science investigations on a dataset emulating a global mission. The campaign deploys NASA's "classic" Airborne Visible Near-Infrared Imaging Spectrometer (AVIRIS-C) over large areas of California. Repeated overflights reveal seasonal as well as interannual changes. The large data volumes provide a unique opportunity to develop algorithms for global measurements. There are three steps to HyspIRI Preparatory Campaign data processing. The "Level 1" algorithm applies radiometric corrections to transform raw instrument Digital Numbers (DNs) into units of radiance. Orthorectification transforms the spectra into 18 m, 30 m and 60 m georeferenced images similar to potential future VSWIR products. Finally, a "Level 2" algorithm corrects for atmospheric effects, estimating anisotropic surface reflectance (or over water, surface-leaving reflectance).

This paper focuses on the atmospheric correction step, with several advances that reduce reflectance artifacts for specific applications. Our method is based on the ATmospheric REMoval (ATREM) algorithm (Gao & Goetz, 1990) that has a long heritage of successful use in airborne and orbital imaging spectroscopy. We begin by describing its theoretical basis and enhancements for the campaign, such as

* Corresponding author at: Jet Propulsion Laboratory, California Institute of Technology, 4800 Oak Grove Dr. M/S 158-242, Pasadena, CA 91109 United States. Tel.: +1 818 354 2200.
E-mail address: david.r.thompson@jpl.nasa.gov (D.R. Thompson).

modifications to gas absorption coefficients and new retrievals of pressure altitude. Our principal contribution is an enhanced water vapor estimate using a linearized full-spectrum fit (Gao & Goetz, 1995) that accounts for liquid and ice absorption. Simulations show that conventional methods for estimating water vapor have biases over vegetated and snow-covered terrain, and that the proposed spectral fitting approach reduces these errors. The retrieval simultaneously estimates optical absorption paths for vapor, liquid, and ice phases of water. This reduces biases in the water vapor estimates and provides new products for hydrology studies (Green et al., 2006).

We evaluate the atmospheric correction approach using a representative set of data from the HyspIRI Preparatory Campaign. We hope to answer the following questions:

● What is the stability of reflectance across multiple flightlines?
● How accurate is the resulting reflectance measurement?
● Is the retrieved water vapor correlated with vegetation cover?
● How do the three phases of water vary over time, region and altitude?

We consider 40 flightlines covering a range of altitudes and ecosystems. The flights extend from Santa Barbara, California, to the north side of Yosemite National Park. We evaluate reflectance using a diverse set of ground targets from a low elevation coastal area to a high elevation inland area. Finally, we conclude by discussing the observed trends in water phases and remaining sources of error in the reflectance calculation.

2. Atmospheric correction approach

Atmospheric correction transforms the measured at-sensor radiance to apparent surface reflectance. We will use "reflectance" here in the ordinary sense, referring to an equivalent Lambertian reflectance (Schaepman-Strub, Schaepman, Painter, Dangel, & Martonchik, 2006). Prior atmospheric correction codes include ACORN (Kruse, 2004), FLAASH (Perkins et al., 2012), and ATCOR (Richter & Schläpfer, 2002). Reviews comparing these methods in greater depth are provided by Gao, Montes, Davis, and Goetz (2009) and Kruse (2004). One can also calculate surface reflectance using an iterative optimal estimation, such as the OCO-2 level 2 algorithm (Crisp et al., 2012). This involves synthesizing a Top of Atmosphere (TOA) spectrum that incorporates scattering, surface reflectance and gaseous absorption across multiple layers of a vertical atmospheric column. The error and its derivatives define a nonlinear least squares problem that can be solved by repeatedly generating new spectra and refining the atmospheric state estimate until reaching a local error minimum. These techniques' computational efficiency is improving (O'Dell, 2010), but they require solving the radiative transfer equations many times for each retrieval and thus remain prohibitively slow for applications involving billions of spectra.

The ATmosphere REMoval code, or ATREM (Gao & Goetz, 1990; Gao, Heidebrecht, & Goetz, 1993), forms the basis of an atmospheric correction approach that can be practically applied to HyspIRI Preparatory Campaign data. The coupling effects between gaseous absorption and atmospheric scattering are neglected in ATREM. This simplification is valid for spectral regions where gaseous absorption is weak, or for regions where the scattering effects are small. It is less accurate for low incidence angles, since longer path lengths increase coupling between absorption and scattering. We first calculate an illumination-invariant Top of Atmosphere (TOA) reflectance ρ, defined as:

$$\rho = \frac{\pi L}{F \cos(\theta)}. \tag{1}$$

Here L represents the radiance in W/sr/nm/cm^2 measured by the instrument, and F the solar downward irradiance in W/nm/cm^2 at the top of the atmosphere (Kneizys, Shettle, Abreu, Chetwynd, & Anderson, 1988). Both terms depend on wavelength λ (omitted for clarity). Here θ represents the solar zenith angle. We use the relation:

$$\rho = T_g \left[r_a + \frac{r_s T_d T_u}{(1 - s r_s)} \right]. \tag{2}$$

The symbol T_g is the gaseous transmittance of the atmosphere, r_a represents the total reflectance of the atmosphere along the optical path, r_s is the surface reflectance, T_u and T_d represent upward and downward transmittances (both direct and diffuse). Here s is the spherical albedo of the atmosphere producing an isotropic irradiance at the surface. Technically the reflectance retrieved by the Level 2 algorithm is bi-conical, but the atmospheric correction assumes that the surface is Lambertian. This is a convenient approximation, and is most accurate
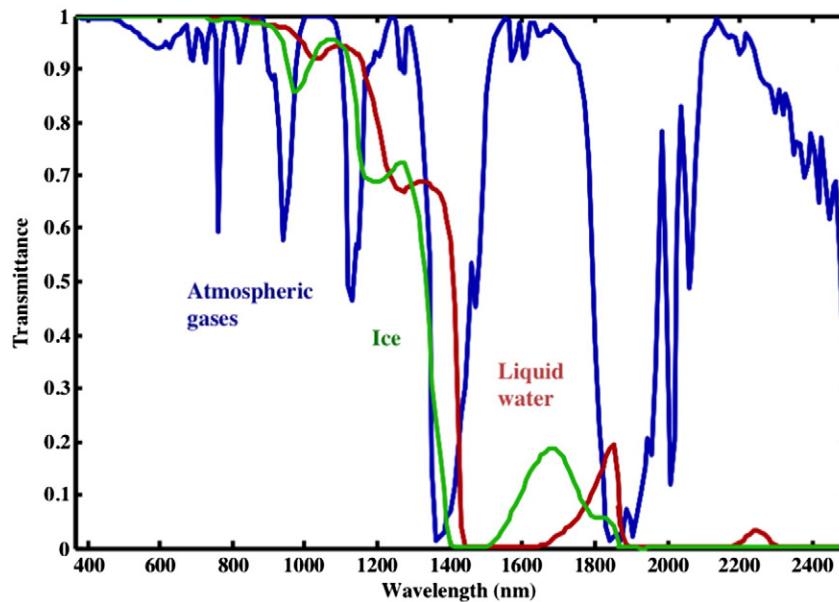
Fig. 1. Transmittance due to atmospheric gases and surface water phases. Ice and liquid water features can distort the shape of the 940 nm and 1140 nm absorption bands used for atmospheric retrievals. Absorption coefficients for liquid water and ice are calculated from their complex indices of refraction (Kou et al., 1993).
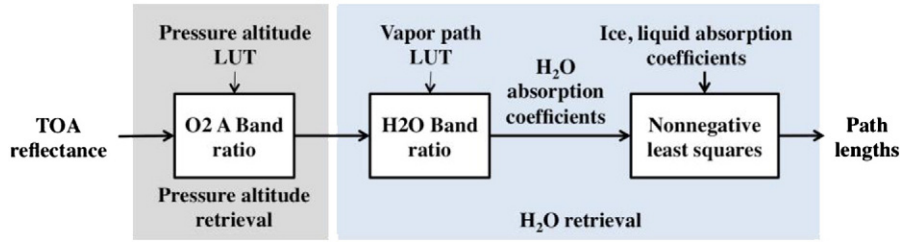
Fig. 2. Procedure for retrieval of pressure altitude and water.

for nadir viewing geometry, low aerosol optical thickness, and low solar zenith angles (Lyapustin, 1999). Solving the equation for surface reflectance yields:

$$r_s = \frac{\rho/T_g - r_a}{T_d T_u + s\left(\rho/T_g - r_a\right)}. \tag{3}$$

This expresses reflectance in terms of gaseous transmittance, aerosol scattering and molecular scattering. We assume aerosol constituents and observation geometry are known. As a result, one can specify free parameters in terms of two unknown atmospheric state variables: the water vapor path and pressure altitude. Consequently we calculate scattering and transmittance coefficients in advance and store them in a two-dimensional lookup table. The table uses 5 pressure altitude levels spaced evenly from 0 to 4 km, and 60 water vapor levels spaced logarithmically from 0 to 5 cm. At runtime we independently estimate each spectrum's atmospheric state and recover the associated coefficients using bilinear interpolation. The following sections detail the calculation of the lookup table, followed by our method for estimating pressure altitude and water vapor values.

2.1. Calculation of scattering and transmittance

Scattering coefficients are calculated from the 6s code (Tanré et al., 1990; Teillet, 1989; Vermote, Tanré, Deuze, Herman, & Morcette, 1997) using a 20-level model atmosphere. AVIRIS-C typically flew under clear conditions, so the scattering calculation uses a fixed aerosol model with a low optical depth (50 km visibility). The particle model is a mixture of three components: 70% dust-like, 29% water soluble, and 1% soot particles. The gaseous transmittance can be written as the product of transmittances of all relevant gases:

$$T_g = T_{H_2O} \, T_{O_2} \, T_{CO_2} \, T_{CH_4} \, T_{CO} \, T_{N_2O}. \tag{4}$$

Abundances of well-mixed gases are effectively constant. Water vapor concentrations are highly variable so this term is usually estimated at runtime from spectral features. The water vapor estimate is not used thereafter to update scattering or foreign broadening of absorption lines, leading to minor inconsistencies when the retrieved vapor differs from the model atmosphere. Nevertheless, this simplification allows the entire procedure to run quickly for many millions of spectra. We note that the equation is most appropriate for calculating the monochromatic vertical transmission of the atmosphere. For the total gaseous transmission averaged over an instrument spectral channel (vertical or slanted), there exist more precise expressions like the k-correlated method of Goody, West, Chen, and Crisp (1989).

We derive atmospheric gaseous transmission with a line-by-line calculation of cross sections from the HITRAN 2012 database (Rothman et al., 2013). Absorption coefficients are calculated for seven model atmospheres, each having 20 atmospheric levels, using the Oxford University Reference Forward Model (Dudhia, 2012). Calculations of self and foreign broadening also assume the model atmosphere. The resulting H_2O absorption coefficients differ slightly from the previous ATREM implementation over the retrieval windows of interest. Flight data revealed a discrepancy between the observed radiance in the 940 nm and 1140 nm water bands over all AVIRIS-C scenes, with unexpectedly high absorption at 1140 nm. This phenomenon has been
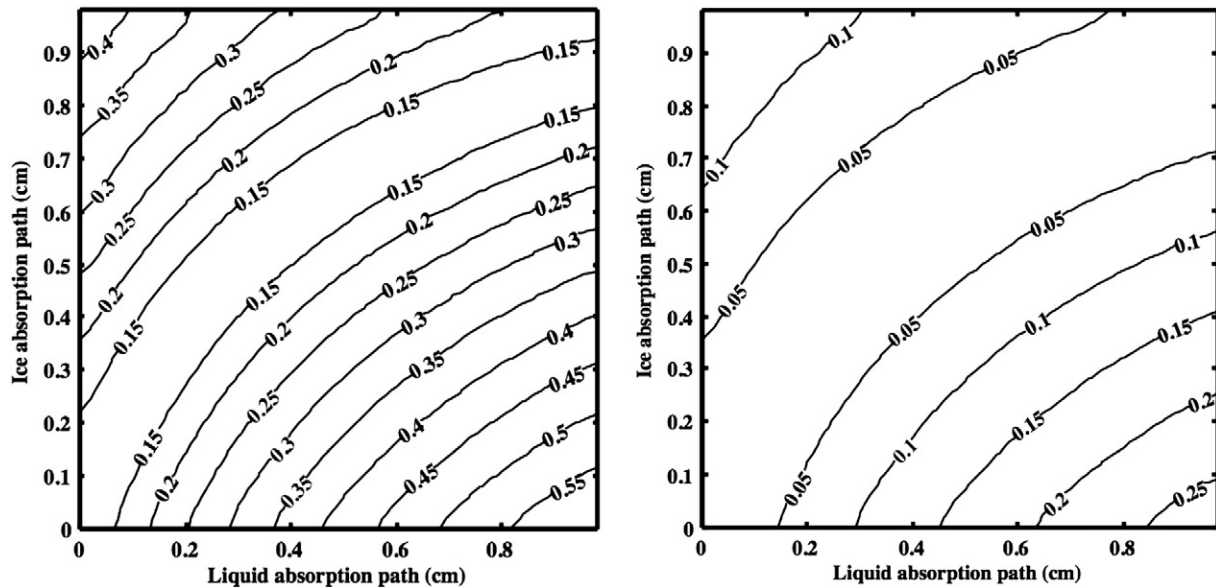

Fig. 3. Mean absolute errors in water vapor estimation (units of cm), over vapor paths from 0 to 2 cm. Axes show actual liquid and ice absorption paths. Left: Errors resulting from a band depth approach. Right: A simultaneous retrieval of three water phases improves accuracy.
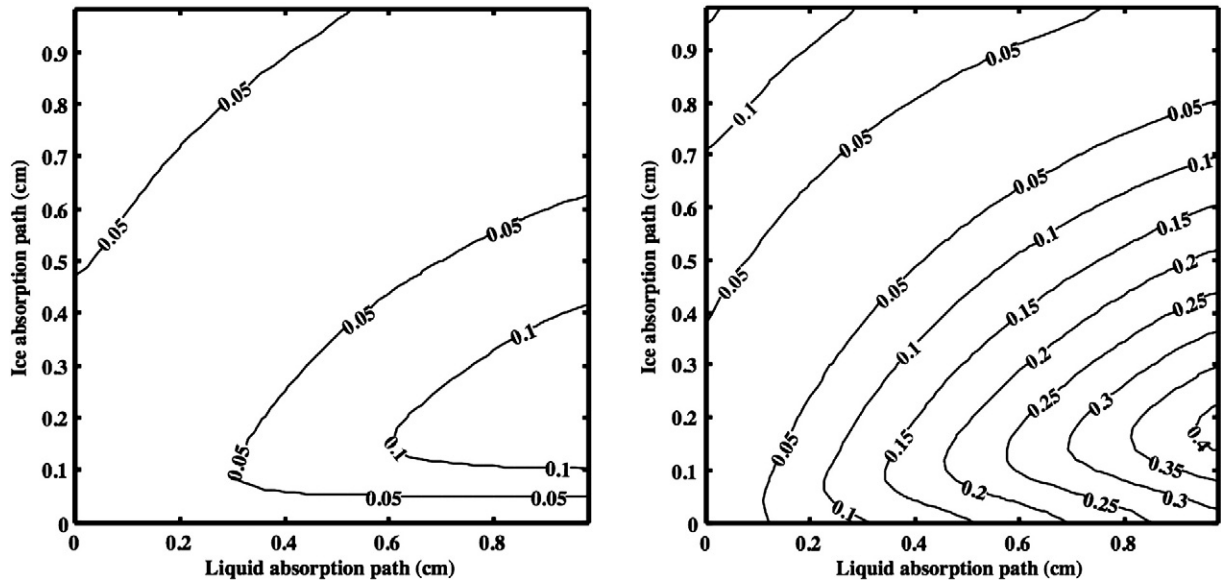
Fig. 4. Contours show mean absolute errors in absorption path length (units of cm). Axes show the actual absorptions of liquid and ice. Errors are averaged over vapor absorption paths from 0–2 cm. Left: Errors in estimates of liquid absorption. Right: Errors in estimates of ice absorption.

observed for many years and multiple versions of water line databases. Here we apply an ad hoc correction by rescaling the absorption cross sections of the stronger 1140 nm band. Retrieving water vapor over a reference scene using each band independently, the answers differ by a ratio of 1.37. We increase the magnitude of the absorption coefficients in the 1140 nm band by this factor, producing a cosmetic improvement in the resulting reflectance spectra.

2.2. Pressure altitude retrieval

Optical path influences the retrieval through aerosol scattering and absorption of well-mixed gases. The HyspIRI Preparatory Campaign, like future orbital instruments, has wide geographic coverage and variable elevation within each image. Consequently we calculate a different optical path for each pixel. One can determine elevation from georectified digital elevation models (Boardman, 1999) but it is operationally simpler to fit absorption features of well-mixed gases. This ensures consistency with the model that will correct the spectrum. Prior work has used the oxygen A band to retrieve pressure altitude (Green, Conel, & Roberts, 1993). We follow a similar approach, with the Continuum Interpolated Band Ratio (CIBR, Green, Carrere, & Conel, 1989) defined by the following expression (Bruegge et al., 1990):

$$R_{CIBR} = \frac{L_m}{\omega_{r1}L_{r1} + \omega_{r2}L_{r2}}. \tag{5}$$

Here R is the ratio of one or more reference measurements from the middle of the absorption feature, denoted L_m, to the continuum level on the right and left sides, written L_{r1} and L_{r2} respectively. Weighting factors ω adjust the contribution of each side based on its distance to the center wavelength. We define the relationship between CIBR and pressure elevation by interpolation in a lookup table. Specifically we simulate model atmospheres that differ in their surface elevations, with candidate elevations spaced regularly from sea level to the aircraft altitude. The atmosphere models have as many as 20 layers (for the case of a surface at sea level). We simulate transmission through each layer, calculate the total absorption due to oxygen by numerical integration, and convolve the instrument response function. This becomes a transmission spectrum whose band depth is assessed for each surface altitude and recorded in the lookup table. Note that, unlike the method of Schläpfer, McCubbin, Kindel, Kaiser, and Ben-Dor (2005), this CIBR

estimate does not account for the path radiance term so it may be less accurate for high aerosol loading or high incidence angles. It proved adequate for the HyspIRI Preparatory Campaign, which generally flew during clear sky conditions.

2.3. Simultaneous retrieval of three phases of water

It is common to estimate column water vapor using the depth of diagnostic spectral absorption features. Liquid and solid states of water have overlapping absorption signatures, so they can interfere with this estimate. Fig. 1 shows an atmospheric transmittance spectrum calculated from HITRAN absorption coefficients, along with ice and
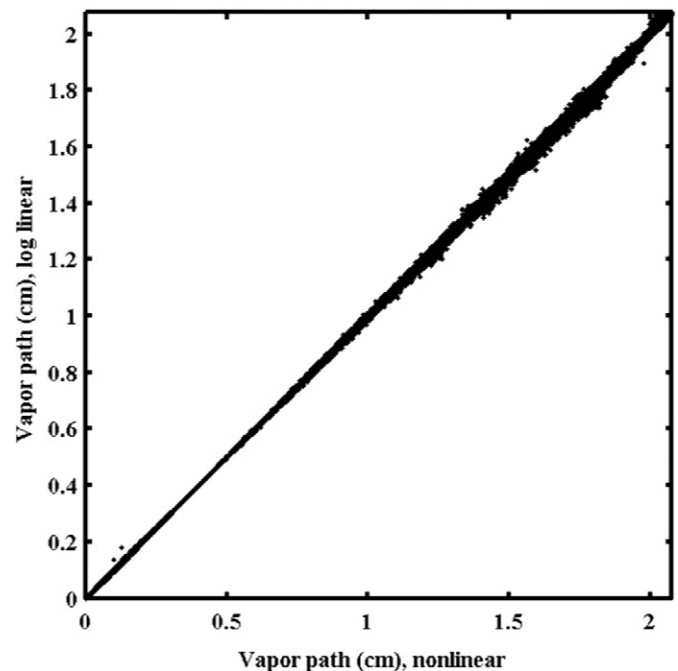

Fig. 5. Comparison of water vapor retrievals using the nonlinear Levenberg–Marquardt solution (horizontal axis) and the linearized solution (vertical axis).
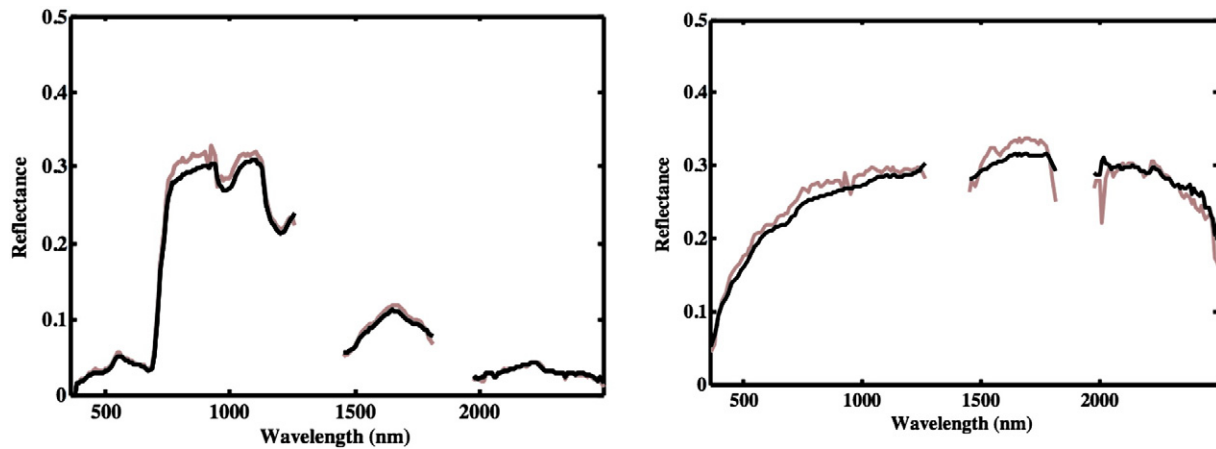
D.R. Thompson et al. / Remote Sensing of Environment 167 (2015) 64–77

Fig. 6. Each plot shows a single pixel from the scene f130503r16. The light red lines indicate the original spectrum, and the bold lines the result after applying correction coefficients. Left: Residual suppression for a typical vegetation spectrum. Right: Exposed granite.

liquid water absorption spectra based on a 3 mm absorption path length. Water vapor features at 940 nm and 1140 nm overlap absorption from liquid water and ice. Consequently water and ice features in these spectral windows can bias the water vapor band depth estimate by violating the assumption of a locally-linear continuum.

We address this with an approach from previous work by Green et al. (2006) that estimates solid, liquid, and gaseous phases simultaneously. This method analyzes the 940 nm or 1140 nm retrieval windows, fitting absorption features of all three water phases. We treat the spectrum as a linear continuum attenuated by the three water absorption components. The model follows from the Beer–Lambert law:

$$\rho(\lambda) = (a + \lambda b) \ \exp[-\sum_j k_j(\lambda)u_j], \quad u_j \geq 0. \tag{6}$$

Here a and b are the offset and slope of the continuum level, with k_j representing the absorption coefficient of each absorber and u_j its nonnegative optical path. Liquid and ice absorption coefficients are calculated from the complex index of refraction (Kou, Labrie, & Chylek, 1993). The vapor absorption coefficient is concentration-dependent due to self broadening, so we perform an initial CIBR retrieval based on the multi-layered transmittance calculation described above. With all absorption coefficients known, one can refine the path lengths and continuum using a nonlinear least squares procedure like the downhill simplex algorithm (Green et al., 2006). Such nonlinear optimization is accurate, but also has some disadvantages. Its computational requirements are inconvenient for large data volumes. It is also somewhat sensitive to initialization conditions and may get stuck in local minima. Here we use a linear approximation of the objective that is both fast and stable. Our approach is inspired by the previous work of Gao and Goetz (1995). We exploit the fact that the exponential function near

zero is almost linear, and that for any line $a + bx$ there exists another line $-g - hx$ such that:

$$a + bx \approx \exp(-g-hx), \quad b \approx 0.$$

The approximation is accurate while a is large relative to bx. For example, if the total change in continuum level is less than 10% of the average over the interval of interest, the approximation is accurate to within 0.1%. This allows the following substitution:

$$\rho(\lambda) = (a + \lambda b) \ \exp\left[-\sum_j k_j(\lambda)u_j\right] \qquad u_j \geq 0$$

$$\rho(\lambda) \approx \exp\left[-l - \lambda m - \sum_j k_j(\lambda)u_j\right] \qquad u_j \geq 0 \tag{7}$$

$$-\log(\rho(\lambda)) \approx l + \lambda m - \lambda n + \sum_j k_j(\lambda)u_j \qquad \{l, m, n, u_j \forall j\} \geq 0.$$

The final line expresses the linear continuum with offset l and slope m as the sum of upward- and downward-trending lines having nonnegative slope coefficients m and n. The new fitting objective is a nonnegative linear least squares problem (Lawson & Hanson, 1974), which is convex and amenable to fast, stable solutions via quadratic programming (Franc, Hlaváč, & Navara, 2005). The speed of our initial implementation is within a factor of 5–10 of a band depth technique. This is sufficient for large-scale operational VSWIR data processing. For even faster execution, an unconstrained unmixing solution based on Singular Value Decomposition would provide a closed-form solution (Gao & Goetz, 1995). Fig. 2 summarizes the steps for retrieving atmospheric state parameters. Our tests suggest that the absorption depth of the oxygen A band is nearly unaffected by water vapor content, so

Table 1
Location, elevation, spatial extent and time of acquisition for the eight calibration targets. Calibration targets were selected to cover a diversity of albedos and surface elevations.

| Target	Latitude	Longitude	Elev (m)	Date	Start (UTC)	End (UTC)	Conditions	Description
Soccer field	34 25.488	− 119 52.315	5.5	2 May 2014	18.15	18.48	Clear	Artificial Turf, 80 m
Parking lot	34 25.625	− 119 51.997	10.4	2 May 2014	18.87	19.28	Clear	USDA lot, 56 m
US post office	34 25.5	− 119 51.865	16.5	2 May 2014	19.88	20.07	Clear	Roof, 60 m
Parking lot	36 32.717	− 119 24.553	104	9 May 2014	19.88	18.73	Part. Cld	Church lot, Dinuba 52 m
Boat ramp	36 51.405	− 119 13.992	277	9 May 2014	20.42	20.95	Part. Cld	Pine Flat Boat Ramp, 9 deg surface, 140 m
Beach	37 13.923	− 119 13.992	2118	10 May 2014	17.73	18	Clear	Huntington Lake 60 m
Rock A	37 03.319	− 119 18.141	1425	10 May 2014	19.84	29.55	Part. Cld	Lichen covered granite, 84 m
Rock B	37 03.364	− 119 18.271	1448	10 May 2014	20.93	21.27	Part. Cld	Lichen covered granite, 112 m
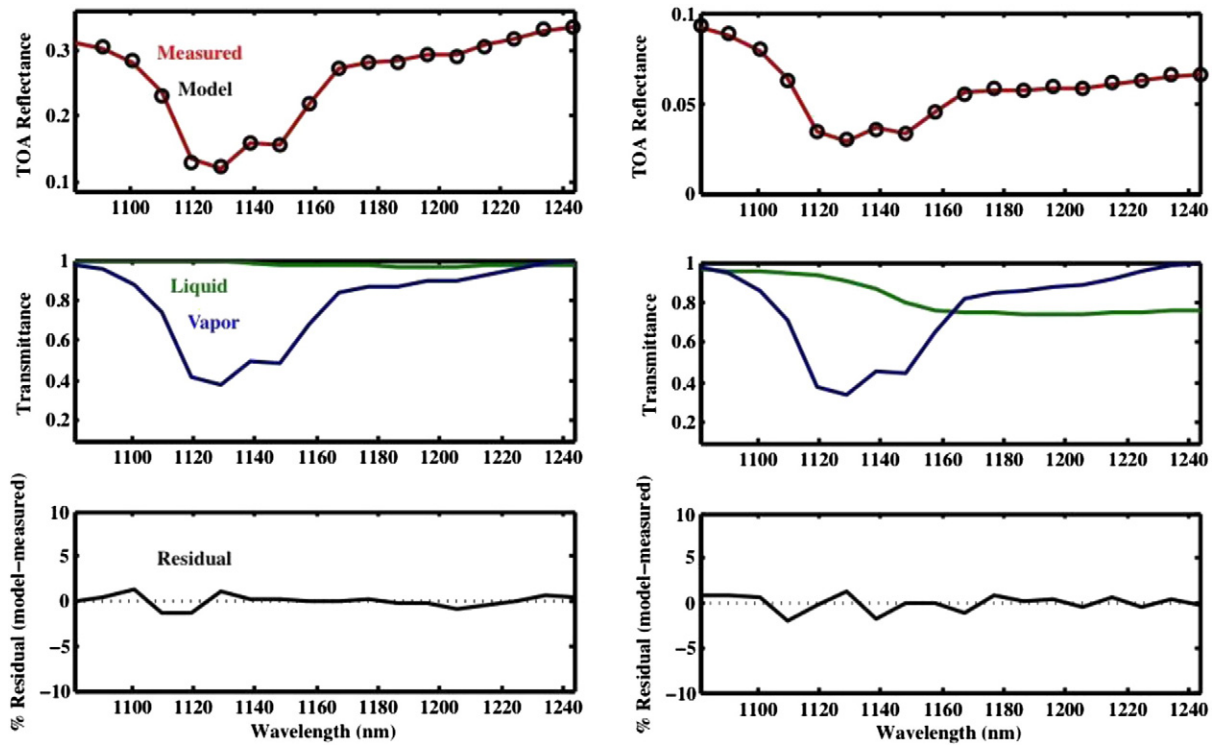
Fig. 7. Typical fit using the linearized three phase retrieval. The retrieval window included the 1140 nm vapor band as well as diagnostic water and ice absorption features. The top row shows measured and modeled spectra. The middle shows estimated transmittances by each component. Residuals are given in the bottom row as a percentage of the maximum TOA reflectance. Left: absorption dominated by water vapor. Right: absorption due to atmospheric features and liquid water.

we retrieve this quantity independently. Next we use the band depth water vapor retrieval to initialize H_2O absorption coefficients; the precalculated Lookup Tables (LUTs) provide transmissions representing total H_2O absorption at all atmospheric layers from which we calculate the absorption coefficient of the equivalent homogeneous atmosphere. Finally, we refine path lengths for all three phases using the nonnegative linear least squares solver.

We evaluated the accuracy of this approach using artificial scenes with known amounts of water as liquid, gas, and ice. We synthesized radiances starting from a reflectance spectrum of "rangeland terrain" from the USGS spectral library. This served as a featureless baseline for adding

absorption. Its slope across the 1140 nm band was approximately 30% of the magnitude making it a challenging case for linearized continuum assumptions. We synthesized radiance spectra by adding absorption from known amounts of liquid and ice, simulating atmospheric scattering and then applying the relation of Eq. (2). We then performed a complete retrieval using the standard band depth technique and proposed atmospheric correction algorithm. For a vapor-only spectrum there was no ambiguity and the retrieval was perfect to within numerical precision. This result degraded as other absorbers were added.

Fig. 3 shows error contours of the vapor estimate, calculated under interference by different amounts of liquid and ice. The traditional
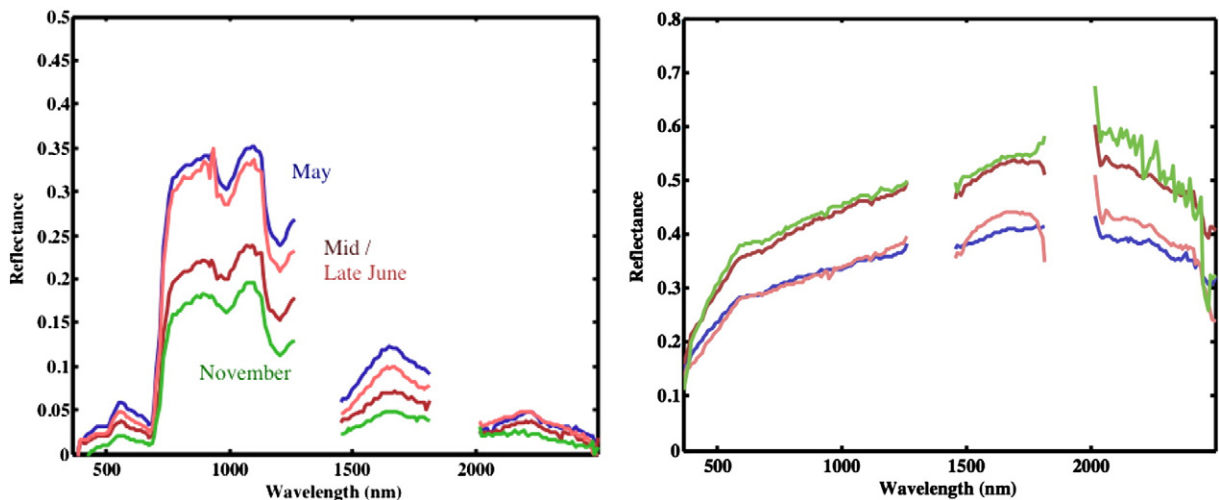

Fig. 8. Vegetation and granite surfaces from the same geographic area across different flights (f130503r16, f130612r08, f130626r11, and f131105r13).

band depth method mis-estimated vapor paths by 0.5 cm or more in the presence of other absorbers. The linearized three-phase retrieval significantly improved these errors. Fig. 4 shows the retrieval error for the linearized three-phase estimates of liquid and ice absorption. When no ice was present, liquid absorption was estimated to better than 0.05 cm accuracy over its entire range of possible values. Small amounts of ice absorption could confuse the retrieval, increasing errors somewhat. These cases would be rare in real physical environments. Ice seems more difficult to estimate, though expanding the retrieval window or adding a second window at 940 nm might help disambiguate the two absorbers. Finally, we evaluated the approximation error given by the difference between the log linear method and the full nonlinear retrieval. The nonlinear solver was initialized with the log linear approach and then further refined using the iterative Levenberg–Marquardt algorithm

(Marquardt, 1963). The log linear water vapor solution matched the nonlinear solution with high accuracy (Fig. 5), but sped execution by over an order of magnitude.

2.4. Residual suppression

After retrieving reflectance spectra and correcting them with Eq. (3), a final step in atmospheric correction compensates for remaining systematic errors due to inaccuracy in calibration, gas absorption coefficients, and solar irradiance. We follow the modified empirical line approach of Moran et al. (2001), fitting a single multiplicative factor to each channel that aligns a direct surface measurement of a spectrally-invariant reference target to the atmospherically-corrected TOA spectrum above that location. Preferred reference targets are flat, bright
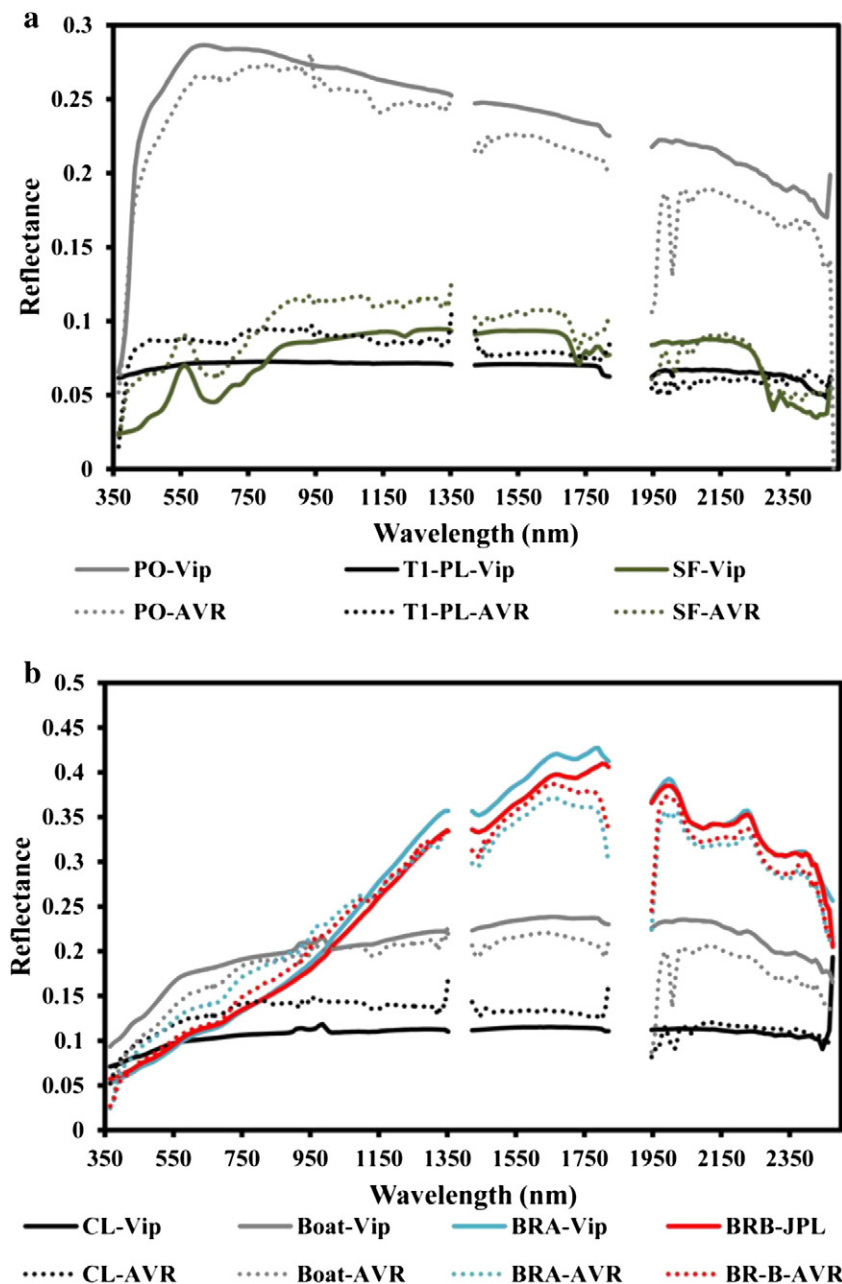
Fig. 9. ASD (solid) and AVIRIS-derived (dotted) reflectance measured along the southern (a) and northern (b) extents of the flight lines. Regions of strong water vapor absorption have been removed from field and AVIRIS reflectance spectra. Spectra include the Post Office Roof (PO), USDA Parking Lot (T1-PL), Soccer Field (SF), Church Parking Lot (CL), Boat Ramp (Boat), Bare Rock A and Bare Rock B (Table 1). The spectrum for the beach at Huntington Lake is not shown because it was snow-covered in April, 2014, but was included in the regression relationship for 2013. Vip refers to the approach in which a spectrum was collected every 4 m, JPL refers to a transect collected using continuous observations (see Methods).

areas such as desert playas used in radiometric calibrations (Green et al., 1998). The resulting coefficients are typically between 0.98 and 1.02, with larger deviations near atmospheric absorption features. This correction factor incorporates all errors introduced by the atmospheric correction, so it would differ from unity even if radiometric calibrations were perfect.
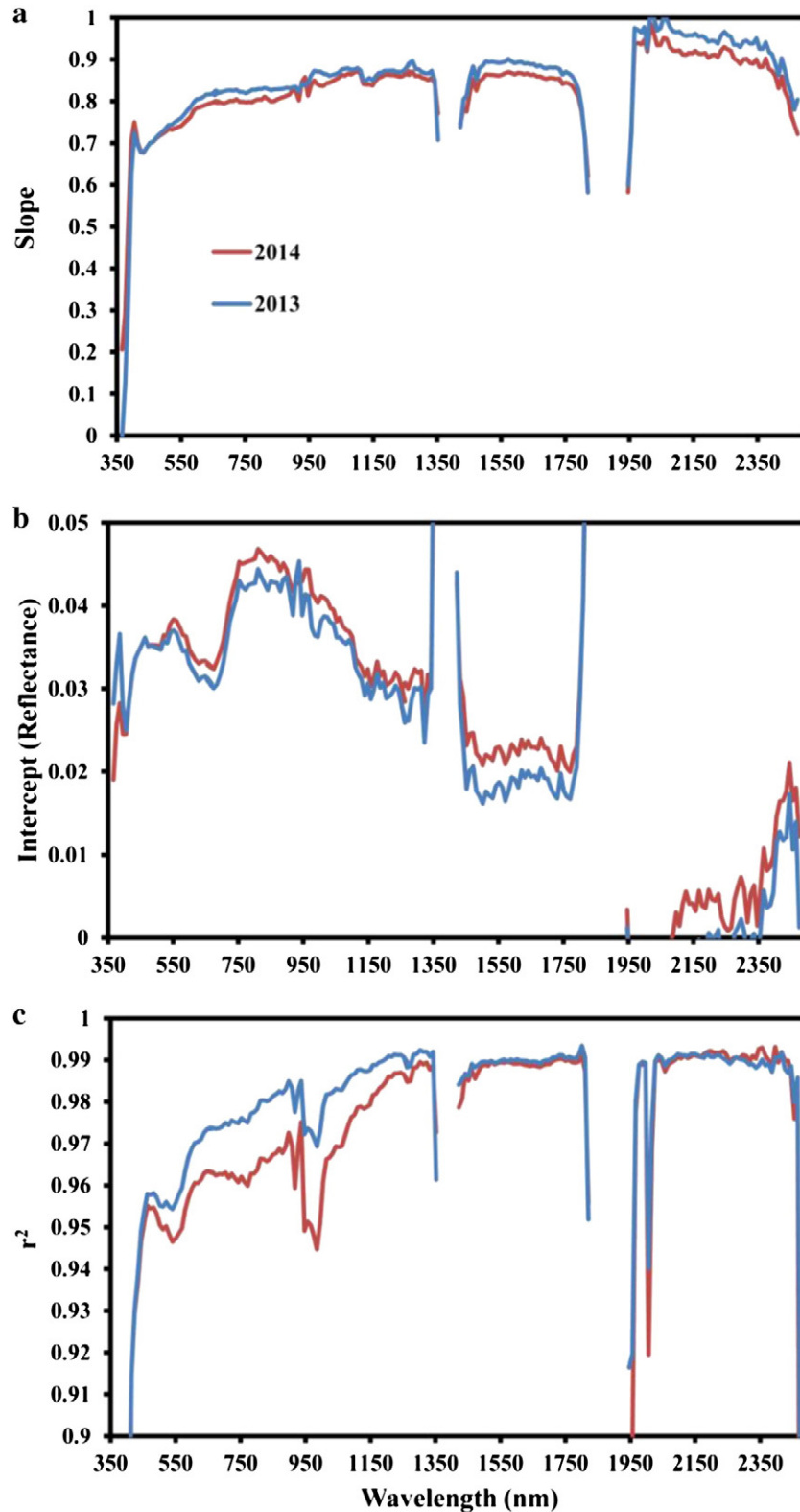
Fig. 10. Plot of slope (a), intercept (b) and rsq (c) in which AVIRIS reflectance (x) was regressed against field reflectance (y). Relationships for 2013 are plotted in blue and relationships for 2014 are plotted in red. All eight targets were used in the 2013 regression, but only seven of eight were used in 2014 due to snow cover on the beach at Huntington Lake.
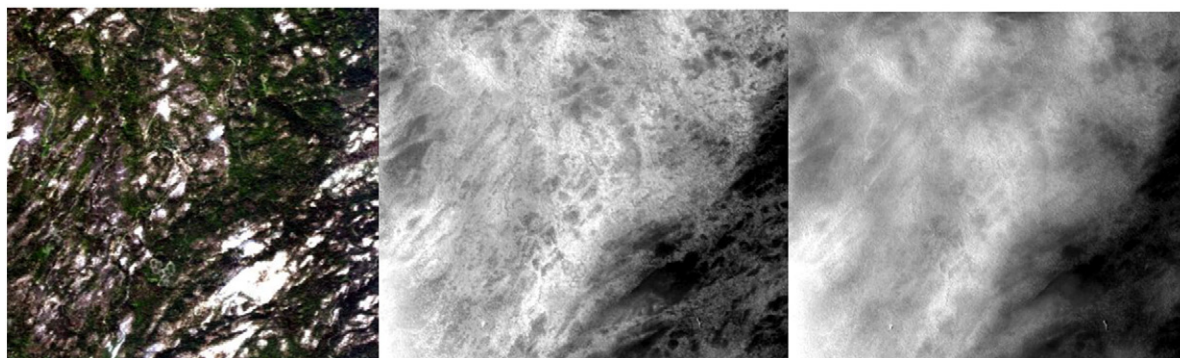
Fig. 11. Left: RGB image of Yosemite park flightline f130503r16. The terrain contains vegetated areas and exposed granite formations. The width of the image is 6.5 km. Center: Water vapor map calculated using the band depth method. Brighter pixels represent more water vapor absorption. Textures indicate interference from surface vegetation. Right: The three phase retrieval produces a more physically-plausible, smooth water vapor map.

In practice we have found these coefficients generalize across different flightlines and even flight days, and correction factors calculated from one scene typically improve reflectance spectra from other flightlines. Fig. 6 below shows an example of two representative materials from the study we will describe in Section 3. Light red lines show the original reflectance estimate, and bold dark lines show the result after residual correction based on a different image and geographic area. The correction smoothes unwanted residuals such as the atmospheric feature near the 940 nm band. In general, it is still best to use correction factors derived from reference measurements close in time, space, and illumination to the image being corrected. But when wide spatiotemporal extent makes this impossible, nonlocal correction factors may still improve results.

3. Experimental data and analysis methods

3.1. Image analysis

This section describes evaluation of reflectance and water retrieved using AVIRIS-C data from the 2013–14 HyspIRI Preparatory Campaign. AVIRIS-C is the closest airborne equivalent to the proposed HyspIRI VSWIR sensor, measuring a spectral range of 350–2500 nm at a spectral sampling of approximately 10 nm. It was mounted on a high-altitude ER-2 aircraft, providing a ground sample distance of approximately 18 m. We used data at full spatial resolution rather than orthorectified data resampled to 30 m or 60 m, in order to avoid geographic mixing effects when evaluating in-situ reflectance.

We analyzed images in an area extending from Santa Barbara, California to the northern limit of Yosemite National Park. This area includes a wide range of altitudes, climatic zones, and ecosystems. The Yosemite area was a challenging subset, which itself contained diverse species, elevations, and water/ice features. This site has been the subject of extensive and ongoing forest ecology and water balance studies (Lutz, van Wagtendonk, & Franklin, 2010), with particular attention to the mixed-conifer ecosystems in the rain–snow transition zone. This

ecosystem is difficult to define precisely, and operational definitions include the elevation range from approximately 1500–2200 m (Bales et al., 2011) or 1800–2500 m (Hunsaker, Whitaker, & Bales, 2012).

The AVIRIS-C flights took place in May, mid and late June, and November of 2013; and April of 2014, providing a range of different snow covers and atmospheric conditions. On each of the acquisition dates the aircraft flew linear flightlines from urban area of Fresno near 600 m elevation to elevated Sierra Nevada peaks at 3000 m and higher. These 38 images provided repeat coverage of over 14,000 km^2. Two additional flightlines transected the entire North/South span extending from the Santa Barbara coast to the Sierra Nevada, providing an additional two degrees of latitudinal range.

We processed raw instrument data using the standard AVIRIS-C data processing pipeline, converting it to calibrated radiance values. Each image was orthorectified using the aircraft built-in GPS/Inertial Measurement Unit measurements and transformed to a regular ground sampling distance using nearest-neighbor resampling. We then performed atmospheric correction using two different water vapor estimates: a traditional band depth estimate, and a linearized three-phase retrieval. Finally, we applied spectral correction factors derived from two overflights of nearby Ivanpah Playa (Green et al., 1998) in early 2013 and 2014. During each overflight a designated area on the playa surface was measured from 400 to 2500 nm at 1 nm resolution with an ASD FieldSpec Pro (Analytical Spectral Devices, Boulder, CO). We converted the resulting spectra to an integrated bi-conical reflectance using a ceramic reference target, and resampled to AVIRIS-C wavelengths for comparison with the remote measurements. We derived a single set of correction factors for each calendar year and applied them to all appropriate flightlines.

3.2. Reflectance validation

We used reference targets to validate the absolute accuracy of the retrieved reflectances, with the ultimate goal of addressing the investigation questions posed in Section 1. Reflectance products were validated

Table 2
Correlations between retrieved water vapor and NDWI as a proxy for canopy water.

Region of interest	Number of pixels	Elevation (m)	Water Retrieval Method	Slope (vapor vs. NDWI)	r-Squared (vapor vs. NDWI)	Slope (Δvapor vs. ΔNDWI)	r-Squared (ΔVapor vs. ΔNDWI)
Farmland	74,000	83	Band depth	0.636	0.676	0.548	0.788
"	"	"	Three phase fit	0.338	0.449	0.256	0.565
Forest	160,000	1806	Band depth	0.362	0.430	0.278	0.572
"	"	"	Three phase fit	0.082	0.109	0.062	0.144
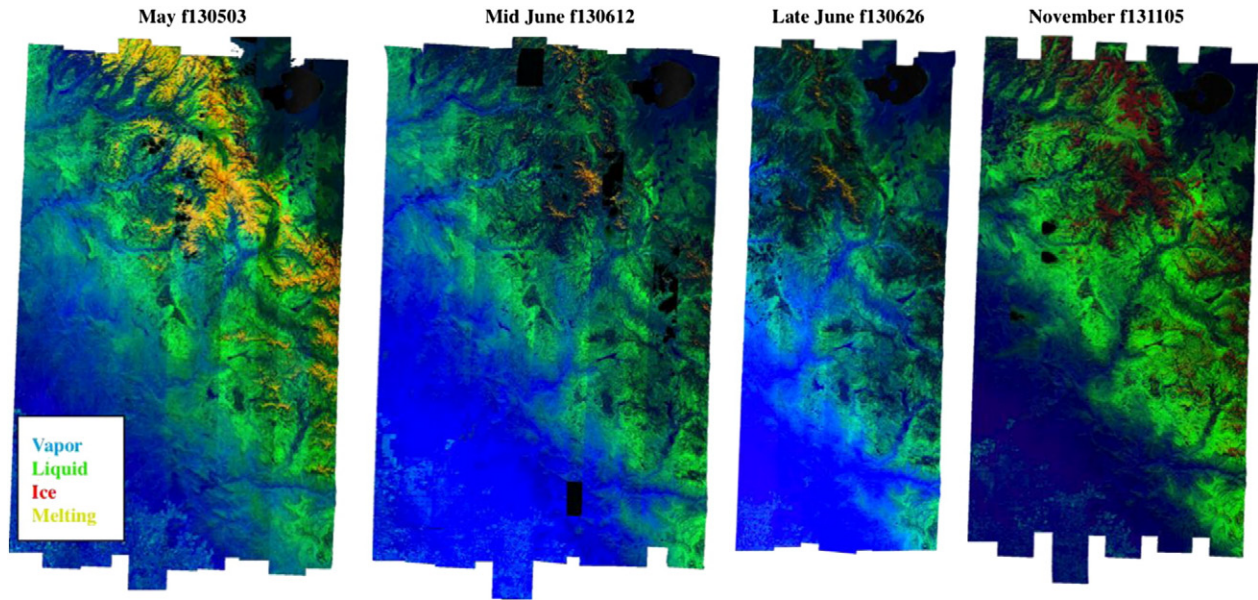
Fig. 12. Mosaics of the Yosemite site acquired on four different dates. Red, green, and blue represent ice, water, and vapor absorption respectively. Yellow pixels contain ice and liquid water, indicating actively melting ice or snow. The ice retrieval has a "noise floor" of approximately 1 mm, and the contrast of these images shows values above this level.

using eight large (>50 m in spatial extent) homogeneous, non-vegetated targets located from the coast to the interior along the AVIRIS-C test images (Table 1). Field reflectance spectra were collected along transects using an ASD full range spectrometer positioned approximately one meter above the surface. No fore optic was used, resulting in an instantaneous field of view of 23° and a circular footprint on the ground with a radius of 0.2 m. All spectra were standardized to a leveled spectralon panel (Labsphere, NH) and collected in reflectance mode. Spectra were collected using two methods, representing dense and sparse sampling of the reference standard. The dense sampling protocol measured groups of five spectra at four meter intervals

with a standard measured every 20 m until the end of the transect was reached. The sparse sampling approach first optimized the instrument, measured a standard, and then measured spectra continuously along the transect collecting one spectrum every three to four paces and concluding the transect with a second measurement of a standard. The latter approach was significantly faster, but also assumed uniform illumination conditions along the transect. To verify no changes in illumination conditions, reflectance spectra of the spectralon panel were compared at each 20 m interval prior to collecting a new standard. With the exception of a high elevation lake target, all spectra were measured within 2 h of solar noon (Table 1). Illumination conditions varied from clear skies on
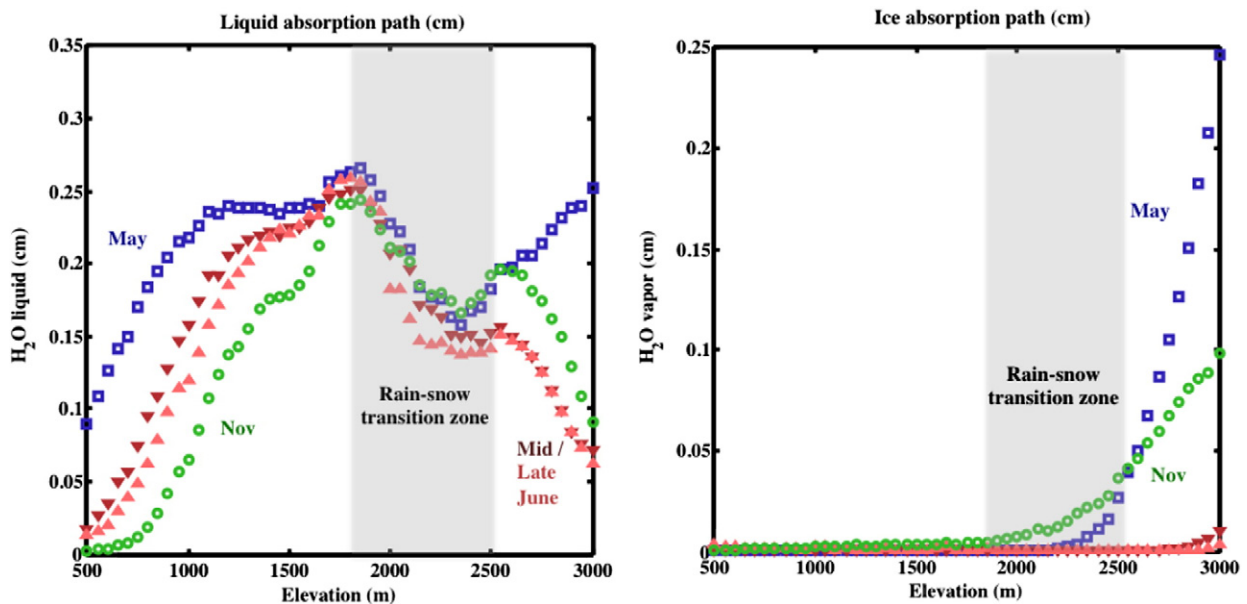
Fig. 13. Liquid, vapor, and ice absorption paths by altitude. The gray region indicates the approximate range of the rain-snow transition zone as studied by Hunsaker et al. (2012).
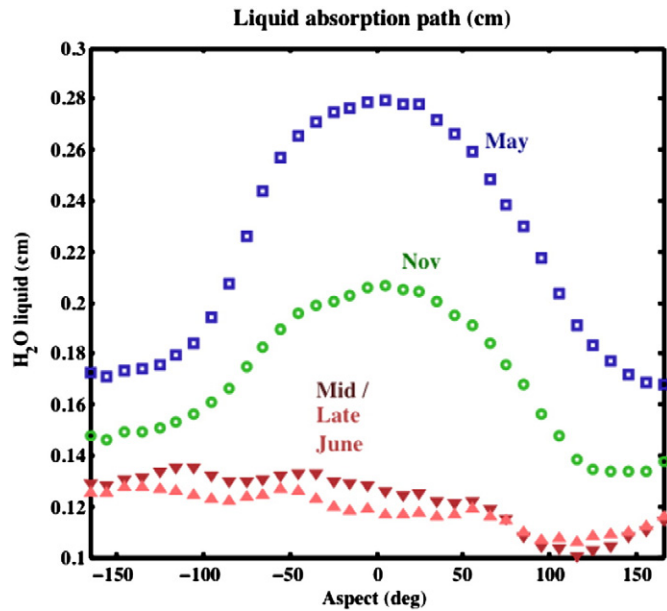
Fig. 14. Liquid absorption paths as a function of aspect angle, for the snow-dominated elevations above 2500 m.

May 2, 2014 to partially cloudy conditions on May 9th and May 10th. The locations of all targets were determined using a GPS unit and verified using high resolution orthoimagery in Google Earth.

Once spectra were acquired, quality was assessed in the laboratory and mean spectra were calculated first as the average of five individual measurements, then as the average of all spectra acquired along a transect. These spectra were then converted to absolute reflectance using the spectrum of spectralon, then convolved to AVIRIS-C using the published wavelength mean and full width half maximum of AVIRIS-C in 2013 and 2014. Calibration targets were located on the May 2, 2013 and April 7, 2014 AVIRIS-C images and mean spectrum of each calibration target was calculated along the corresponding image transect. To assess the quality of retrievals, field and AVIRIS-measured spectra were compared and AVIRIS reflectance was regressed against field measured reflectance for each wavelength to calculate a slope, intercept and r-squared value for each band. Since there are 8 reference targets, the regression models have 8 points per wavelength.

3.3. Evaluation of water retrievals

Next we evaluated the influence of liquid water absorption on retrieved water vapor using a traditional band depth approach and the proposed three phase method. We calculated the Normalized Difference Water Index (NDWI, Gao, 1996 — an established measure of canopy water) for selected vegetated areas and analyzed the linear correlation with the retrieved vapor path. We calculated slope and r-squared values. To guard against possible correlation of canopy water and water vapor over large areas, we compared local changes across neighboring pixels. Specifically we calculated the difference between neighboring pixels' column water vapor (ΔVapor) and their difference in NDWI (ΔNDWI). Over these small distances atmospheric water vapor was expected to be spatially homogeneous and independent from surface properties. It followed that any correlation between ΔNDWI and ΔVapor would represent an unwanted bias.

Finally, we characterized the three phases of water over time, region and altitude. We examined the resulting absorption path products as mosaic maps, anticipating results similar to Green et al. (2006) in which water vapor was controlled mainly by topography while liquid water was associated with vegetation. We expected ice absorption paths to follow seasonal Sierra Nevada snow cover trends, with a depletion of the snow pack during the spring and a snow/ice transition boundary at altitudes from 1800–2500 m.

4. Results

4.1. Image analysis results

Over typical terrain, the three phase model of $\rho(\lambda)$ matched AVIRIS-C measurements to within 1–2% (Fig. 7). Reflectances across different Yosemite flights were consistent in shape though their magnitude varied. Fig. 8 shows vegetation and granite spectra from the same geographic location in May, Mid- and Late-June, and November. Minor changes in the magnitude of the reflectance spectrum were expected due to variable illumination direction and intensity that can alter the appearance of microtexture (for the granite surface) and canopy self-shading (for vegetation). Tree leaf Bidirectional Reflectance could also
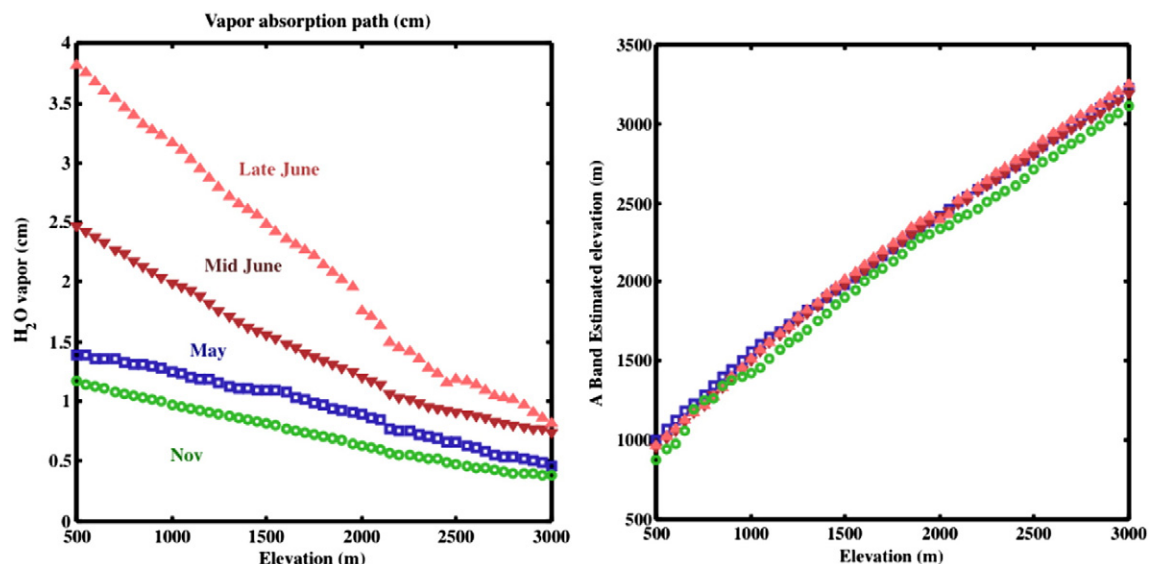

Fig. 15. Left) Retrieved vapor path length as a function of elevation. Right) Retrieved pressure altitude as a function of elevation.

have played a role. Despite these differences, the spectral shape remained constant over all flightlines and particularly stable for the granite reference.

4.2. Reflectance validation results

Reflectance was further validated using eight homogeneous ground targets located along the light lines (Fig. 9). In general, AVIRIS-derived reflectance was within several percent of field measured reflectance. There was a general pattern of AVIRIS-derived reflectance being slightly lower than field measured reflectance, resulting in a slope between 0.8 and 0.9, for 2013 and 2014 respectively (Fig. 10a). Poorest correlations were observed at the shortest wavelengths and in strong water vapor bands, located at 940, 1350 and 1900 nm (Fig. 10c). Correlations did not degrade at 1130 nm. One of the most significant artifacts was a positive bias, expressed as an intercept in the regression relationship as high as 0.045 in 2013 and 0.035 in 2014. The intercept had a pronounced spectral shape, including a broad peak at blue to green wavelengths (420 to 600 nm), a dip at 657 nm and a broad peak centered at 850 nm. At wavelengths greater than 850 nm, the intercept declined, approaching zero by 2000 nm. We discuss these results at greater length in Section 5.

4.3. Water retrieval results

We inspected the resulting water vapor maps for vegetation-induced biases. Two representative rectangular regions of interest were selected from the Yosemite flightline f130502r19. The first was low elevation developed area with both planted and fallow agricultural fields. The second was a wilderness area at higher altitude, containing areas of both forested and bare terrain. Biases were apparent in the band depth version as visual textures aligning with vegetated areas. In contrast, the three phase retrieval produced a smoother and more physically-plausible vapor map (Fig. 11). Table 2 shows the correlation coefficients between liquid and vapor phases for each retrieval approach. Stronger correlations were observed in the difference quantities (ΔVapor and ΔNDWI) than in absolute values. The three phase retrieval outperformed the band depth method by this metric. It reduced the slope and r-squared values in every case: from 0.788 to 0.565 (Farmland) and from 0.572 to 0.144 (Forest). This indicates an imperfect but improved decorrelation of vapor and surface liquid.

Next, we characterized spatiotemporal trends in the water maps. We formed orthorectified mosaics of all 38 Yosemite flightlines (Fig. 12). We found that water vapor paths followed topography, while liquid was related to the presence of vegetation, and ice appeared at high altitudes. This agreed with previous findings by Green et al. (2006). Repeat coverage over time further revealed temporal phenomena including the summer retreat of ice and fresh unmelted snow in November images. We quantified these trends, binning pixels according to elevation (Fig. 13). Water absorption paths showed at least three different seasonal trends at different elevations, aligning with rain-dominated regions below 1800 m, the transition zone of Hunsaker et al. (2012); and snow-dominated area above 2500 m. Lower elevations dried out during early summer (Bales et al., 2011) showing gradual reduction in leaf canopy water. Liquid water at higher elevations was associated with snow and ice. Significant snow and ice was observed above the transition boundary.

Finally, we examined the relationship between water absorption paths and topography. The Mid and Late June overflights showed an asymmetrical distribution of snow in the zone between 2500 m and 3000 m, with the most water on northeast-facing slopes (Fig. 14). The May and November distributions added a symmetrical component centered at due north, possibly linked to melting snow. Fig. 15 shows the relationship between elevation and atmospheric state parameters (e.g. water vapor and pressure altitude). Pressure altitude was nearly

linear with altitude with a consistent bias ranging from approximately 5% at 1000 m to less than 2% at 3000 m elevation. This discrepancy might be related to errors in O_2 A band absorption coefficients, or to the exclusion of scattering from the CIBR calculation. The water vapor path was observed to vary more dramatically across flightlines, with a strong inverse relationship to altitude.

5. Discussion

Global mapping spectrometers will require atmospheric correction that functions accurately and consistently without analyst intervention. This requires reliable automatic performance over diverse terrain and imaging conditions. To our knowledge, this effort is the first systematic validation of automatic VSWIR reflectance products against multiple ground truth measurements over a wide geographic and altitude range. Regression analysis reveals a high correlation between the field and remote measurements (r-squared above 0.95) but also systematic biases in the form of a positive intercept and a slope less than 1. The positive intercept is somewhat similar to a plant spectrum, consistent with adjacency effects that our algorithm does not currently correct. The bias does not exactly mimic vegetation reflectance (it has a peak red absorption at 657 nm rather than 680 nm) and may be caused by a combination of factors. In general the reflectance product underestimates the reflectance of bright targets and overestimates the reflectance of dark targets. This bias has systematic wavelength dependence consistent with undercorrection for atmospheric scattering at short wavelengths (Fraser & Kaufman, 1985). We note that the retrieval uses a low aerosol optical depth of 0.12, in contrast with direct atmospheric measurements that commonly report higher values (Kahn, Gaitley, Martonchik, Diner, & Crean, 2005). This makes automatic retrieval of aerosol parameters an important next step toward a fully automatic atmospheric correction approach. A bias in retrieved pressure altitude by 200–500 m may also contribute to underestimation of molecular scattering.

The validation also points to continuing challenges in the alignment of 940 nm and 1140 nm water band strengths. It suggests that a single multiplicative adjustment is not a perfect fix, since vapor estimates from the 1140 nm band imperfectly correct the 940 nm region. This effect reduces correlation with ground truth at 940 nm, and occasionally leaves visible residual artifacts in reflectance spectra. The discrepancy is present across a wide range of materials. It could be related to uncertainties in the intensity of line absorption coefficients, self-broadened continuum contributions, or other unmodeled spectroscopic effects like differential influence of the aerosols on the gaseous path lengths.

The validation process could be refined further. Great care was taken with the ground truth protocol, but additional measurements by another in-situ instrument would add confidence that the observed differences are due entirely to the airborne retrieval. We cannot completely exclude other potential contributors from the surface data collection including minor imperfections in the spectralon reference, differences in the Instantaneous Field of View (IFOV), and non-Lambertian properties sensitive to the slight solar zenith differences between airborne and ground-based acquisitions.

The flight data corroborates our simulations, in which accounting for liquid and ice phases of water improves atmospheric water vapor estimates. Traditional band depth retrievals rely on a continuum that is linear near diagnostic absorption features. When absorbers at the surface violate this assumption it impacts both atmospheric correction and downstream users of water vapor maps. Ice and liquid water are the most common offenders. Fortunately, their distinct signatures permit a simultaneous retrieval. A variant of Gao and Goetz's log-linear method (1995) provides fast, stable solutions with good accuracy over parameter ranges of interest. Our evaluation uses maps of Yosemite ranging over 3000 m of elevation and 15,000 km^2 in extent. These reveal expected accumulation of liquid and ice phases, and seasonal trends that vary along accepted hydrological zones such as the rain-snow

transition. To date, studies have characterized water balance (Lutz et al., 2010), and plant and soil moisture (Bales et al., 2011) with combinations of in-situ sampling and meteorological data. Remote sensing may contribute further with wide-area data on plant physiological variables such as leaf water content (Cheng, Zarco-Tejada, Riaño, Rueda, & Ustin, 2006; Cheng, Riaño, & Ustin, 2014; Fuentes, Gamon, Qiu, Sims, & Roberts, 2001; Serrano, Ustin, Roberts, Gamon, & Penuelas, 2000). Quantitatively validating water vapor retrievals could be more challenging, since there is significant 3D spatial variability and the optical path from sun to sensor is difficult to reproduce with a second validation instrument. Nevertheless LIDAR atmospheric probing or meteorological sounding could contribute to a more thorough validation of these products.

6. Conclusion

Accurate atmospheric correction will be a key enabling technology for future global VSWIR mapping spectrometers. The HyspIRI Preparatory Campaign's reflectance data processing pipeline uses a variant of the ATREM atmospheric correction algorithm. It includes modifications to absorption cross sections, a new pixelwise retrieval of pressure altitude, and water vapor estimation based on a linearized simultaneous spectral fit of absorption to three water phases. We characterized agreement between airborne and ground-based spectra in two different years using a variety of different targets and elevations. We also examine the resulting water products, and find that the three-phase retrieval improves the water vapor retrieval in the presence of liquid absorption features. The retrieval provides new products that measure the distribution of water at high spatial resolution, with additional value for hydrology studies. Initial products suggest the system's ability to resolve known hydrological features, such as the rain-snow transition zone, based on the seasonal trends associated with different altitude ranges.

Acknowledgements

References

Bales, R.C., Hopmans, J.W., O'Geen, A.T., Meadows, M., Hartsough, P.C., Kirchner, P., et al. (2011). Soil moisture response to snowmelt and rainfall in a Sierra Nevada mixed-conifer forest. *Vadose Zone Journal, 10*(3), 786–799.

Boardman, J.W. (1999, February). Precision geocoding of low altitude AVIRIS data: lessons learned in 1998. *AVIRIS 1999 Proceedings* (pp. 63–68).

Bruegge, C.J., Conel, J.E., Margolis, J.S., Green, R.O., Toon, G.C., Carrere, V., et al. (1990, September). In-situ atmospheric water-vapor retrieval in support of AVIRIS validation. *Imaging Spectroscopy of the Terrestrial Environment. International Society for Optics and Photonics.* (pp. 150–163).

Cheng, T., Riaño, D., & Ustin, S.L. (2014). Detecting diurnal and seasonal variation in canopy water content of nut tree orchards from airborne imaging spectroscopy data using continuous wavelet analysis. *Remote Sensing of Environment, 143*, 39–53.

Cheng, Y.B., Zarco-Tejada, P.J., Riaño, D., Rueda, C.A., & Ustin, S.L. (2006). Estimating vegetation water content with hyperspectral data for different canopy scenarios:

Relationships between AVIRIS and MODIS indexes. *Remote Sensing of Environment, 105*(4), 354–366.

Crisp, D., Fisher, B., O'Dell, C., Frankenberg, C., Basilio, R., Bosch, H., et al. (2012). The ACOS CO2 retrieval algorithm—part II: global XCO₂ data characterization. *Atmospheric Measurement Techniques, 5*(4), 687–707.

Dudhia, A. (2012). Oxford University Reference Forward Model (RFM). http://www.atm.ox.ac.uk/RFM/

Franc, V., Hlaváč, V., & Navara, M. (2005, January). Sequential coordinate-wise algorithm for the non-negative least squares problem. *Computer Analysis of Images and Patterns* (pp. 407–414). Heidelberg: Springer Berlin.

Fraser, R.S., & Kaufman, Y.J. (1985). The relative importance of aerosol scattering and absorption in remote sensing. *IEEE Transactions on Geoscience and Remote Sensing, GE-23*(5), 625–633.

Fuentes, D.A., Gamon, J.A., Qiu, H.L., Sims, D.A., & Roberts, D.A. (2001). Mapping Canadian boreal forest vegetation using pigment and water absorption features derived from the AVIRIS sensor. *Journal of Geophysical Research – Atmospheres (1984–2012), 106*(D24), 33565–33577.

Gao, B.C. (1996). NDWI—a normalized difference water index for remote sensing of vegetation liquid water from space. *Remote Sensing of Environment, 58*(3), 257–266.

Gao, B.C., & Goetz, A.F. (1990). Column atmospheric water vapor and vegetation liquid water retrievals from airborne imaging spectrometer data. *Journal of Geophysical Research – Atmospheres, 95*(D4), 3549–3564.

Gao, B.C., & Goetz, A.F. (1995). Retrieval of equivalent water thickness and information related to biochemical components of vegetation canopies from AVIRIS data. *Remote Sensing of Environment, 52*(3), 155–162.

Gao, B.C., Heidebrecht, K.B., & Goetz, A.F. (1993). Derivation of scaled surface reflectances from AVIRIS data. *Remote Sensing of Environment, 44*(2), 165–178.

Gao, B.C., Montes, M.J., Davis, C.O., & Goetz, A.F.H. (2009). Atmospheric correction algorithms for hyperspectral remote sensing data of land and ocean. *Remote Sensing of Environment, 113*(S1), S17–S24.

Goody, R., West, R., Chen, L., & Crisp, D. (1989). The correlated-k method for radiation calculations in nonhomogeneous atmospheres. *Journal of Quantitative Spectroscopy and Radiative Transfer, 42*(6), 539–550.

Green, R.O., Carrere, V., & Conel, J.E. (1989). Measurement of atmospheric water vapor using the Airborne Visible/Infrared Imaging Spectrometer. *Proc. ASPRS Conference on Image Processing, Reno, NV.*

Green, R.O., Conel, J.E., & Roberts, D.A. (1993). Estimation of aerosol optical depth, pressure elevation, water vapor, and calculation of apparent surface reflectance from radiance measured by the airborne visible/infrared imaging spectrometer (AVIRIS) using a radiative transfer code. *Optical Engineering and Photonics in Aerospace Sensing. International Society for Optics and Photonics.* (pp. 2–11).

Green, R.O., Eastwood, M.L., Sarture, C.M., Chrien, T.G., Aronsson, M., Chippendale, B.J., et al. (1998). Imaging spectroscopy and the airborne visible/infrared imaging spectrometer (AVIRIS). *Remote Sensing of Environment, 65*(3), 227–248.

Green, R.O., Painter, T.H., Roberts, D.A., & Dozier, J. (2006). Measuring the expressed abundance of the three phases of water with an imaging spectrometer over melting snow. *Water Resources Research, 42*(10), W10402.

Hook, S.J., & Oaida, B.V. (2010). *NASA 2009 HyspIRI Science Workshop Report* (pp. 10–13). Jet Propulsion Laboratory Publication (Available at http://trs-new.jpl.nasa.gov/dspace/handle/2014/41511).

Hunsaker, C.T., Whitaker, T.W., & Bales, R.C. (2012). Snowmelt Runoff and Water Yield Along Elevation and Temperature Gradients in California's Southern Sierra Nevada. *JAWRA Journal of the American Water Resources Association, 48*(4), 667–678.

Kahn, R.A., Gaitley, B.J., Martonchik, J.V., Diner, D.J., & Crean, K.A. (2005). Multiangle Imaging Spectroradiometer (MISR) global aerosol optical depth validation based on 2 years of coincident Aerosol Robotic Network (AERONET) observations. *Journal of Geophysical Research, 110*(D10S04), 1–16.

Kneizys, F.X., Shettle, E.P., Abreu, L.W., Chetwynd, J.H., & Anderson, G.P. (1988). *Users Guide to LOWTRAN 7 (No. AFGL-TR-88-0177)*. Hanscom AFB, MA: Air Force Geophysics Lab.

Kou, L., Labrie, D., & Chylek, P. (1993). Refractive indices of water and ice in the 0.65-to 2.5-μm spectral range. *Applied Optics, 32*(19), 3531–3540.

Kruse, F.A. (2004). Comparison of ATREM, ACORN, and FLAASH atmospheric corrections using low-altitude AVIRIS data of Boulder, CO. *13th JPL Airborne Geoscience Workshop. 05–3,* . Jet Propulsion Laboratory Publication (10 pp.).

Lawson, C.L., & Hanson, R.J. (1974). *Solving Least Squares Problems.* Englewood Cliffs, NJ: Prentice-hall, 161.

Lutz, J.A., van Wagtendonk, J.W., & Franklin, J.F. (2010). Climatic water deficit, tree species ranges, and climate change in Yosemite National Park. *Journal of Biogeography, 37*(5), 936–950.

Lyapustin, A.I. (1999). Atmospheric and geometrical effects on land surface albedo. *Journal of Geophysical Research, 104*(D4), 4127–4143.

Marquardt, D.W. (1963). An algorithm for least-squares estimation of nonlinear parameters. *Journal of the Society for Industrial and Applied Mathematics, 11*(2), 431–441.

Moran, M.S., Bryant, R., Thome, K., Ni, W., Nouvellon, Y., Gonzalez-Dugo, M.P., et al. (2001). A refined empirical line approach for reflectance factor retrieval from Landsat-5 TM and Landsat-7 ETM+. *Remote Sensing of Environment, 78*(1), 71–82.

O'Dell, C.W. (2010). Acceleration of multiple scattering, hyperspectral radiative transfer calculations via low streams interpolation. *Journal of Geophysical Research – Atmospheres (1984–2012), 115*(D10).

Perkins, T., Adler-Golden, S., Matthew, M.W., Berk, A., Bernstein, L.S., Lee, J., et al. (2012). Speed and accuracy improvements in FLAASH atmospheric correction of hyperspectral imagery. *Optical Engineering, 51*(11), 111707-1–111707-7.

Richter, R., & Schläpfer, D. (2002). Geo-atmospheric processing of airborne imaging spectrometry data. Part 2: atmospheric/topographic correction. *International Journal of Remote Sensing, 23*(13), 2631–2649.

Rothman, L.S., Gordon, I.E., Babikov, Y., Barbe, A., Chris Benner, D., Bernath, P.F., et al. (2013). The HITRAN2012 molecular spectroscopic database. *Journal of Quantitative Spectroscopy and Radiative Transfer, 130*, 4–50.

Schaepman-Strub, G., Schaepman, M.E., Painter, T.H., Dangel, S., & Martonchik, J.V. (2006). Reflectance quantities in optical remote sensing—definitions and case studies. *Remote Sensing of Environment, 103*(1), 27–42.

Schläpfer, D., McCubbin, I.B., Kindel, B., Kaiser, J.W., & Ben-Dor, E. (2005). Wildfire smoke analysis using the 760 nm oxygen absorption feature. *4th EARSeL Workshop on Imaging Spectroscopy, Warsaw* (pp. 1–10).

Serrano, L., Ustin, S.L., Roberts, D.A., Gamon, J.A., & Penuelas, J. (2000). Deriving water content of chaparral vegetation from AVIRIS data. *Remote Sensing of Environment, 74*(3), 570–581.

Tanré, D., Deroo, C., Duhaut, P., Herman, M., Morcrette, J.J., Perbos, J., et al. (1990). Technical note description of a computer code to simulate the satellite signal in the solar spectrum: the 5S code. *International Journal of Remote Sensing, 11*(4), 659–668.

Teillet, P.M. (1989). Surface Reflectance Retrieval Using Atmospheric Correction Algorithms. *Geoscience and Remote Sensing Symposium. IGARSS'89. 12th Canadian Symposium on Remote Sensing. 2.* (pp. 864–867).

Vermote, E.F., Tanré, D., Deuze, J.L., Herman, M., & Morcrette, J.J. (1997). Second simulation of the satellite signal in the solar spectrum, 6S: An overview. *IEEE Transactions on Geoscience and Remote Sensing, 35*(3), 675–686.